ELSEVIER

Catalysis Today 69 (2001) 385–392

CATALYSIS TODAY

www.elsevier.com/locate/cattod

Liquid and gas flow and related phenomena in monolithic catalysts studied by ^{1}H NMR microimaging

Igor V. Koptyug [a,*], Ludmila Yu. Ilyina [a], Anatoly V. Matveev [a], Renad Z. Sagdeev [a], Valentin N. Parmon [b], Stephen A. Altobelli [c]

[a] *International Tomography Center, Institutskaya Str. 3A, Novosibirsk 630090, Russia*
[b] *Boreskov Institute of Catalysis, Pr. Akademika Lavrentieva 5, Novosibirsk 630090, Russia*
[c] *New Mexico Resonance, 2301 Yale Blvd., SE, Suite C-1, Albuquerque, NM, USA*

Abstract

NMR is employed to study liquid and gas flow in a tube and in the channels of shaped catalysts, mass transport during drying of water saturated porous monoliths, and gas adsorption by porous alumina pellets. NMR flow imaging and pulsed field gradient NMR are shown to yield the same average propagators for liquid and gas flow in a straight circular tube. The complicated patterns of gas or liquid flow in shaped reactors are characterized successfully by NMR flow imaging through the detection of all three flow velocity components.

Keywords: ^{1}H NMR; Microimaging; Alumina; Fluid flow; Monolith

1. Introduction

Heat and mass transport processes are crucial for heterogeneous catalysis. One of the ways to control these processes is to use catalyst/support pellets with a well-defined shape. The shape of the catalysts and supports can have a major impact on the efficiency of a catalytic process through its effect on flow and mixing through the reactor. For instance, implementation of monolithic catalysts possessing large transport channels allows one to uniformly distribute flow and to reduce pressure drop across a reactor [1,2]. The information on mass transport in liquid and gas flow in shaped catalysts can be utilized to improve their performance. Therefore, systematic studies of mass transport in shaped catalysts and reactors are highly desirable.

NMR has been widely used to characterize diffusion of gases [3–9] as well as diffusion and flow of liquids [10–20] in a variety of geometries for a long time. However, applications in heterogeneous catalysis are few [13,21], and until recently the technique was not employed to study fluid flow in shaped catalysts. A number of applications of gas NMR imaging to materials science have been reported, both with hyperpolarized [8,22] and thermally polarized gases [5,23,24]. However, gas flow imaging was not addressed at all until 1999 [22,25]. The application of dynamic NMR imaging of hyperpolarized ^{129}Xe to obtain two-dimensional spatial maps of flow velocity distribution for a tube with a constriction and for two types of polyurethane foams is reported in [22]. We have demonstrated recently that thermally polarized gases such as acetylene, propane and butane at the atmospheric pressure are amenable to NMR gas flow imaging at moderately high (e.g., 7 T) magnetic fields [25] (vide infra). New and promising studies of this

* Corresponding author. Tel.: +7-3832-333-561; fax: +7-3832-331-399.
E-mail address: koptyug@tomo.nsc.ru (I.V. Koptyug).

0920-5861/01/$ – see front matter
PII: S0920-5861(01)00396-0

type are emerging in the fields of materials science and catalysis.

In this work, we have applied NMR microimaging to study the flow of liquids and gases and other types of mass transport processes in shaped catalysts. The aim of this study is to demonstrate the feasibility and potential usefulness of such applications and to compare the results obtained for liquid and especially gas flow by NMR flow imaging and pulsed field gradient (PFG) NMR.

2. Techniques

A number of NMR techniques exist which can be employed to study flow phenomena both qualitatively and quantitatively [10,26]. NMR flow imaging provides spatially resolved picture of the flow patterns. The spatial maps of all three flow velocity components can be obtained. A different approach to the characterization of flow by NMR is based on the PFG experiment [11,15–17]. This approach is employed successfully to detect certain average characteristics of motion, such as $P(z, \tau)$, the probability for a molecule to be displaced by the distance z in time τ, sometimes called an 'average propagator'. If the velocity V of the molecule does not change within the measurement time (a few to a few hundred ms), i.e., $z = V\tau$, the two approaches are expected to yield equivalent results. The important difference with the flow imaging approach is that the PFG NMR experiment can be employed even if there is no net flow in the object, i.e., to study diffusive displacements of spins including the case of restricted diffusion in porous materials [12–14]. Furthermore, this approach can provide direct information on flow dispersion coefficient, e.g., for fluids flowing in porous materials.

3. Experimental

Propane gas was purchased from a commercial vendor. Distilled water was used in the water flow studies. For the studies of water or gas flow in a circular tube, a single, 5–6 m long piece of flexible plastic tubing with 7.6 mm i.d. was used, with the measurements performed on its straight section. For the studies of fluid flow through various monoliths, a 21 mm i.d. cylindrical Teflon cell was employed to accommodate the roughly cylindrical pieces of the monoliths.

During the gas flow experiments, the gas was expanding from the tank into the supply tubing and was leaving the setup through the open end of the exhaust tubing into the fume hood. The flow of water was created by a thermostat pump. In all experiments, water, propane or dry air entered the sample cell at the bottom and left at the top.

A number of monolithic structures made of γ-Al_2O_3 with the straight channels of different geometry were used in the experiments. Most of the studies were carried out with the monolith which had a specific surface area of 62 m^2/g and 14 nm average pore diameter. It had transport channels of $4 \times 4\ mm^2$ square cross-section and wall thickness of 1 mm and was 50 mm long. In some experiments it was placed on top of another monolith with smaller channels ($1 \times 1\ mm^2$, wall thickness 0.2 mm). Other experiments were done with a cylindrical monolith which had six approximately triangular channels separated by 2 mm walls. For all monoliths, the orientation of the channels was coincident with the direction of the cylindrical cell axis.

All ^{1}H NMR microimaging experiments were performed at 299 MHz on a Bruker DRX spectrometer equipped with a vertical bore superconducting magnet. The spin-echo pulse sequence was employed in all flow imaging experiments. The echo time was 2.7 ms for water and 5.1 ms for gas flow imaging. The 2D images were detected in the plane perpendicular to the cell axis. The slice thickness was 2 mm for water and 15 or 4 mm for gas studies. Two extra gradients were applied along the z-axis to phase encode the flow velocity [26]. The field of view was 24 mm^2 in all experiments. Each 2D data set was zerofilled to 256×256 prior to 2D Fourier transformation. It took 20–40 min to acquire each 2D image.

PFG NMR experiments were performed using the spin-echo pulse sequence with echo time 8.1 ms (water) or 4.7 ms (propane). In some cases, slice selection along the direction of the main flow was used to reduce the influence of the inflow/outflow effects on the signal amplitude.

The 1D single point imaging (SPI) technique [27,28] was employed to map the distribution of a fluid within a porous solid both in the monolith drying

experiments and in the imaging of propane adsorbed on a single alumina pellet.

4. Results and discussion

The first set of experiments deals with the water and gas flow imaging in a well-defined geometry — a straight section of a circular tube. Fig. 1a shows the spatial distribution of the axial flow velocity component in the transverse cross-section of such tube for water flowing at $Re = 285$ ($Re = ud/\nu$ is the Reynolds number, u the average flow velocity, d the tube diameter, and ν the kinematic viscosity). The 1D cross-section of the flow map along the tube diameter is superimposed on the map. It is fitted with a parabola (solid line) to demonstrate the excellent agreement of the experimental results with the expected behavior.

Fig. 1c shows the results of the same experiment, but with the Reynolds number of water flow $Re = 1825$. In this case, the flow velocity distribution is distorted, and the 1D cross-section clearly deviates from a parabola. Under conditions of this experiment we estimate the entrance length to be of the order of 42 cm, which is comparable to the length of the straight section of the tube. The geometry of the vertical superconducting magnet requires the tube to bend as it enters the magnet from below. We therefore conclude that the figure shows the flow pattern which is not fully developed, since the Re number is too low for an onset of turbulence to be observed. The NMR method is sensitive to unsteadiness in the flow and our results indicate that this flow was steady, which further indicates this was a developing and not a transitional flow.

Fig. 1e shows the result of the propane gas flow imaging experiment at $Re = 580$. It is obvious that despite a much lower signal/noise ratio and a much higher diffusivity of gas as compared to water, a good quality flow map with a parabolic cross-section is obtained. While this result may appear trivial, the validation of the flow imaging technique for the case of gas flow was never attempted. Therefore, this experiment is essential to ensure that reliable conclusions can be drawn from the further gas flow studies.

Next, based on the flow maps obtained, we have constructed the histograms of the velocity probability distribution $P(V)$ (Fig. 1b, d and f, solid line), and compared those to the $P(z/\tau)$ measured directly by PFG NMR (dashed line). The results are in a very good agreement for both water and propane at different Re numbers. Nevertheless, some differences between the solid and dashed curves can be seen. The direct PFG measurement of $P(V)$ clearly underestimates the P-values at higher velocities because some spins leave the sensitive volume of the RF coil or the volume of the selected slice during the pulse sequence [20]. The fresh spins flowing into the sensitive volume after the first RF pulse do not contribute to the detected signal. The higher the velocity is, the larger fraction of spins leave the sensitive volume within the duration of the pulse sequence. Therefore, the directly detected $P(V)$ plots are skewed toward higher velocities, and this distortion becomes more pronounced at higher Re numbers. The histograms, on the other hand, are constructed by counting pixels of the flow maps and therefore are not affected by the inflow/outflow effects directly. The inflow/outflow effects should be less of a problem in the porous media flow studies.

It can be seen in Fig. 1f that the histogram (solid line) has steeper edges as compared to the $P(V)$ measured directly by PFG NMR (dashed line), because the latter is sensitive to diffusive motion of spins as well. This effect becomes pronounced for gases due to their large diffusivity values ($6.5 \times 10^{-2}\,\mathrm{cm}^2/\mathrm{s}$ for propane at 20°C and atmospheric pressure).

It should be noted, however, that NMR flow imaging becomes impractical for channel diameters less than 50 μm for liquid flow NMR experiments since the spatial resolution can be improved only at the expense of the signal/noise ratio. For thermally polarized gases, the signal/noise ratio is much lower, and the practical channel diameter limit is of the order of 0.5–1 mm. For smaller channels and pores, the direct detection of $P(z)$ or $P(V)$ is thus the only option available, and the comparison of the two techniques indicates that the reliable results can be expected.

In the next set of experiments, we have employed NMR flow imaging to visualize flow patterns of water and protonated gases flowing through the channels of monolithic catalysts. Fig. 2 shows 2D flow velocity maps detected transverse to the direction of the monolith channels at various distances from the inflow edge of the monolith. The flow velocity component directed along the channels is visualized. Also shown in Fig. 2 are the 1D cross-sections of the 2D flow velocity maps. The experiment was performed

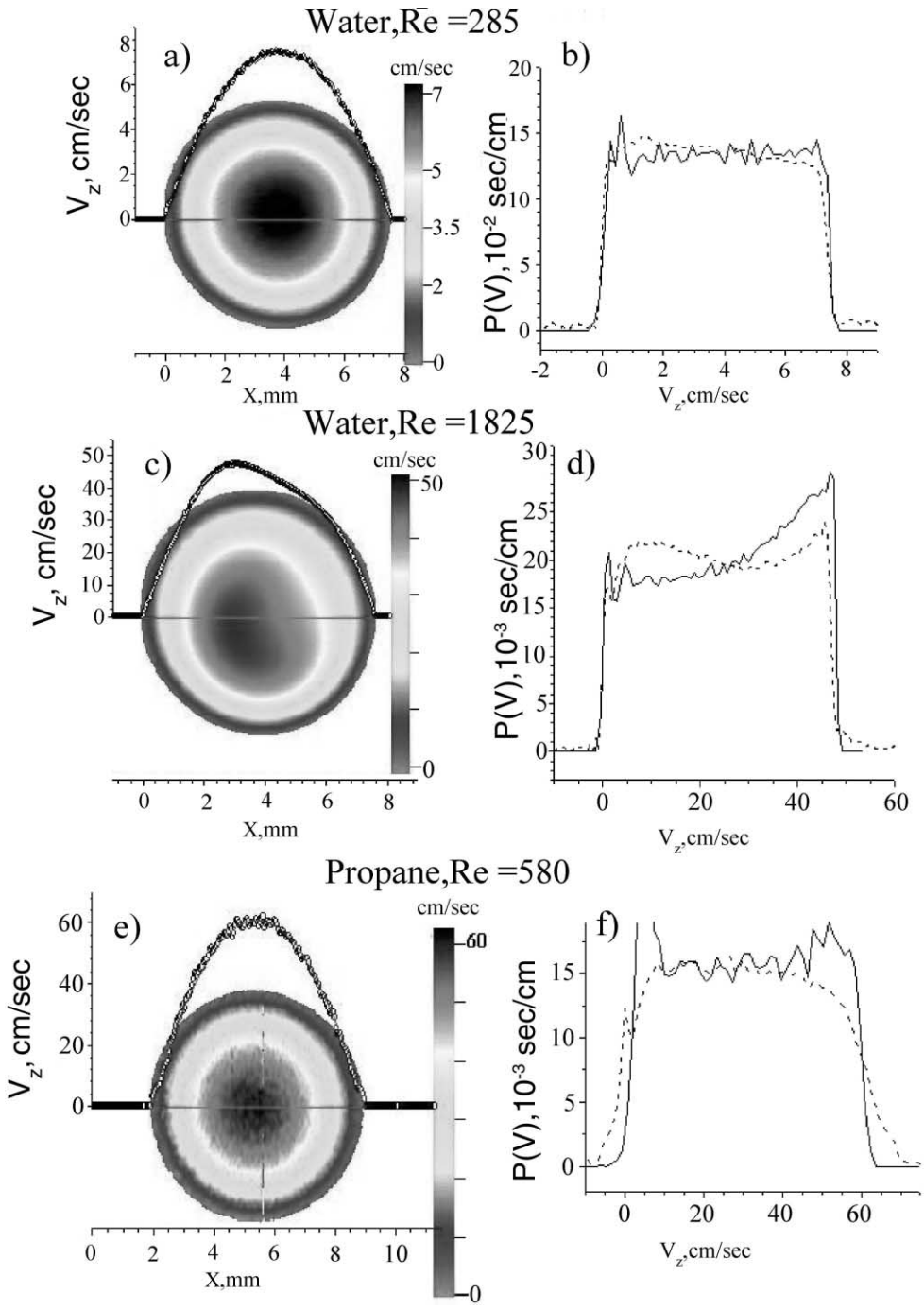

Fig. 1. Two-dimensional flow maps showing the spatial distribution of the flow velocities for water (a) and (c) and propane (e) in a circular tube, with one-dimensional horizontal cross-sections superimposed. All 2D maps show the velocity component perpendicular to the image plane, and zero velocity level of the 1D cross-section defines the position of the cross-section relative to the 2D map. The probability distribution $P(V)$ calculated from the flow maps ((b), (d) and (f), solid line) and the same quantity measured directly (dashed line) are shown.

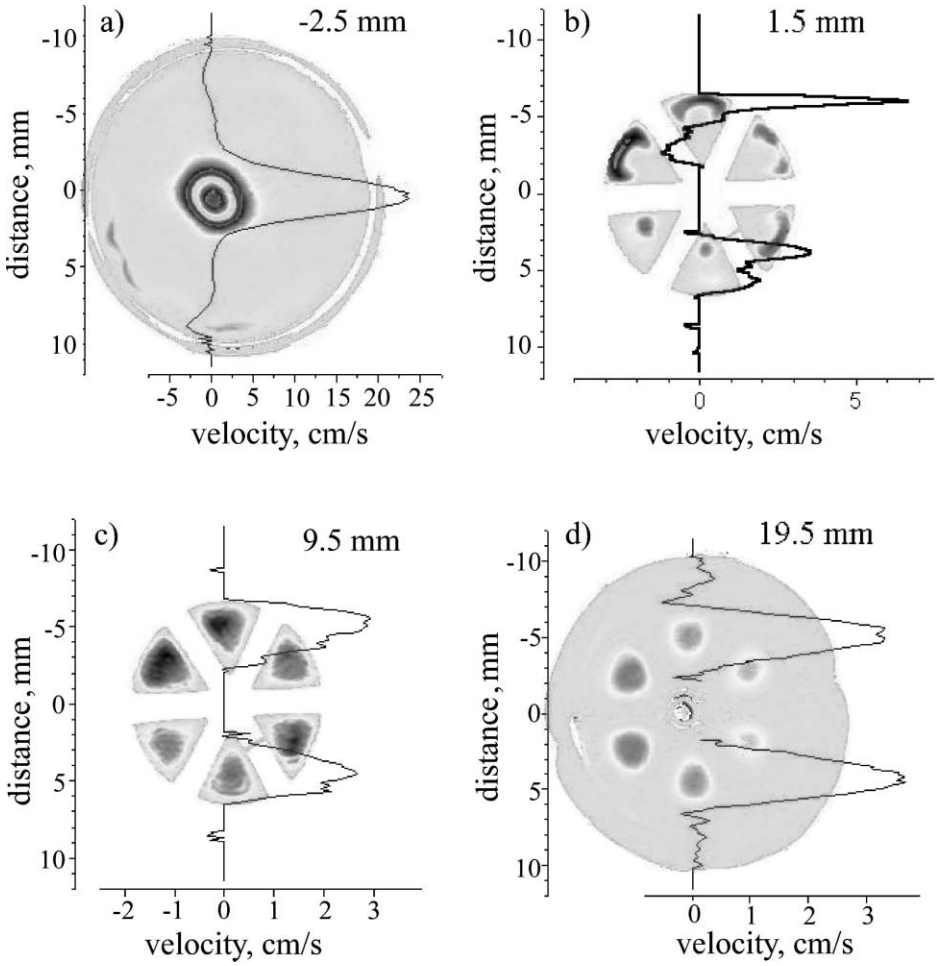

Fig. 2. Two-dimensional flow maps showing the spatial distribution of water flow velocities in a cylindrical cell containing a monolith with triangular channels, with the one-dimensional cross-sections superimposed. The 2D maps were detected at various distances from the inflow edge of the monolith. These distances are indicated in the figure, with the negative values corresponding to the cross-sections outside the monolith. The length of this monolith was 18 mm, i.e., the map in (d) is detected downstream of the monolith.

with a single monolith possessing six channels with a triangular cross-section. It was placed in a cylindrical cell 20 mm above the bottom edge of the cell, with the cell axis coincident with the axis of the monolith and parallel to the direction of its transport channels. Water inflows into the cell at the bottom through the narrow supply tubing approximately along the axis of the sample (central peak in Fig. 2a). As the stream approaches the lower edge of the monolith, it separates into several parts entering the channels of the monolith (positive peaks in Fig. 2b). Four of the streams (Fig. 2b) are roughly crescent-shaped, while in the two other channels the flow pattern is somewhat different, presumably due to the deviations of the geometry of the experiment from cylindrically symmetric one. As the streams proceed further along the channels they gradually expand to fill out the entire cross-section of the channels (Fig. 2c). Eventually, the developed flow pattern is established. Since this monolith was only 18 mm long, it was also possible to visualize the six streams after they leave the monolith at the top (Fig. 2d). A low signal intensity area in the center of the

flow map of Fig. 2d implies the likely presence of vortices in this region. Furthermore, the flow maps clearly reveal the presence of recirculating flows in the direction opposite to that of the main flow in various regions (negative peaks in Fig. 2a and b).

A similar experiment was performed with a monolith possessing channels with a square cross-section. Similar to the results shown in Fig. 2, the flows in the entrance regions of four central channels are crescent-shaped, and the reverse flows exist near the inner corners of the channels and upstream of the inflow edge of the monolith. In order to make water flow through the monolith channels more uniform, we have placed another monolith with narrower channels under the first monolith. Its structure is apparent in the flow map shown in Fig. 3a. In this case, the

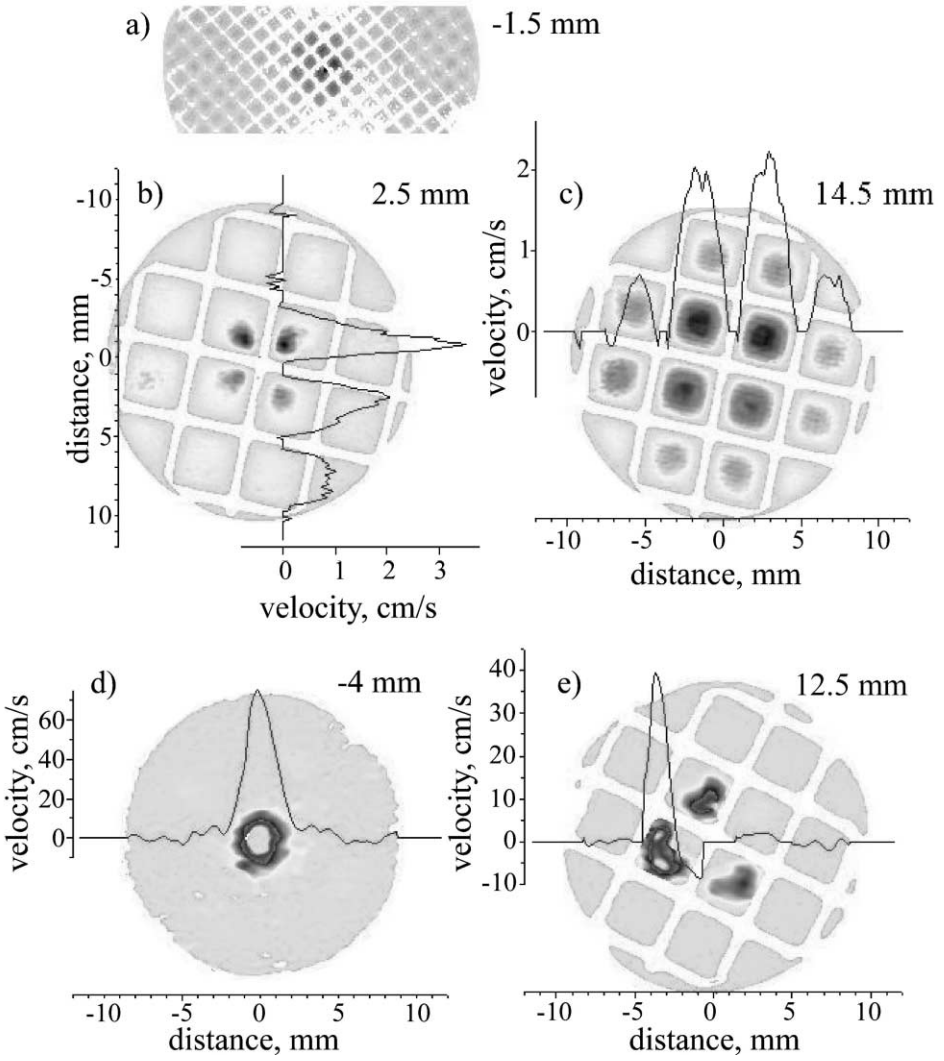

Fig. 3. (a)–(c) Same as in Fig. 2, but with the main monolith with square channels supported by an additional monolith with narrower channels. The structure of the latter is apparent in (a), where only part of the cylindrical sample is shown. (d) and (e) Two-dimensional flow maps showing the spatial distribution of propane flow velocities in a cylindrical cell containing the same monolith (no support). Propane flow rates are 236 ml/min (d) and 400 ml/min (e). The distances from the inflow edge of the monolith are indicated in the figure, with the negative values corresponding to the cross-sections outside of the monolith.

stream first enters the monolith with narrower channels (Fig. 3a) and then separates into four streams entering the wider channels of the other monolith. The major difference with the previous geometry is that now the four streams enter the monolith near the inner corners of the four central channels. Besides, there is much more flow through the outer channels of the monolith in the latter case.

We have demonstrated recently that thermally polarized gases such as acetylene, propane and butane at the atmospheric pressure are amenable to NMR gas flow imaging at moderately high (e.g., 7 T) magnetic fields [25]. The 2D flow maps of these gases flowing in the channels of the monoliths (*Re* numbers 190–570) were detected within a reasonable experimental time (30–90 min) with a true in-plane spatial resolution of 400 μm × 400 μm. An example of the propane flow maps are shown in Fig. 3d and e. Despite a lower signal/noise ratio as compared to water images, the results are encouraging. The flow patterns observed are similar to those of water, including the presence of reverse flows (Fig. 3e). A detailed discussion of the gas flow imaging results can be found elsewhere [25].

It should be noted that despite a relatively high fluid content in the porous walls of the monoliths (porosity ca. 0.25), the images detected show no NMR signal within the walls. The reason is a much shorter spin–spin relaxation time T_2 of fluids within the porous material and a strong T_2-weighting of the signals detected with the spin-echo pulse sequence employed. Utilization of an SPI pulse sequence [27,28] allowed us to demonstrate strong adsorption of propane within alumina catalysts. NMR imaging can thus be employed to study the dynamics of gas adsorption and desorption processes.

Furthermore, NMR imaging can provide useful information on mass transport of liquids, and possibly gases, both within the porous walls of the shaped catalysts (internal mass transport) and across the gas/solid interface at the channel walls of the catalyst (external). As an example, we have studied the process of drying of the alumina monolith, initially saturated with water, by a stream of dry air passing through its channels [29]. The results demonstrate an efficient capillary redistribution within the porous walls in the course of the drying process. Work is currently in progress to extract mass transfer parameters from the experimental data.

5. Conclusions

This work demonstrates that NMR imaging can be successfully employed to study the flow of liquids and gases in structured catalysts and reactors. It is shown that the results obtained by NMR flow imaging and PFG NMR are mutually consistent for both liquid and gas flow. NMR flow imaging technique allowed us to fully characterize the complicated flow pattern upstream, inside and downstream of the monolith, and to reveal the presence of the recirculating flows in the regions of significant rearrangement of the main streams. The obtained flow maps provide direct access to the information on shear rates which affect the external mass transfer rates in porous systems. The variation of the flow pattern along the channels of the monolith affects the local rate of mass transfer across the monolith/gas interface during drying of a prewetted monolith. Finally, it is demonstrated that NMR imaging can be employed to visualize the protonated gases adsorbed within porous materials and to study the dynamics of adsorption process.

Acknowledgements

The collaboration between the International Tomography Center and New Mexico Resonance was supported by a NATO Collaborative Linkage grant No. PST.CLG 975244. IVK thanks the Russian Foundation for Basic Research (project No. 99-03-32314a) and the Siberian Division of the Russian Academy of Sciences for financial support. A.V. Matveev acknowledges a scholarship awarded by the Zamaraev International Charitable Scientific Foundation. Additional support by the Engineering Research Program of the Office of Basic Energy Sciences, US Department of Energy, under Grant No. DE-FG03-98ER14912 is acknowledged.

References

[1] F. Kapteijn, J.J. Heiszwolf, T.A. Nijhuis, J.A. Moulijn, CATTECH 3 (1999) 24–41.
[2] J. Votruba, O. Mikus, K. Nguen, V. Hlavacek, J. Skrivanek, Chem. Eng. Sci. 30 (1975) 201–206.
[3] R.W. Mair, D.G. Cory, S. Peled, C.-H. Tseng, S. Patz, R.L. Walsworth, J. Magn. Reson. 135 (1998) 478–486.

[4] M. Pfeffer, O. Lutz, J. Magn. Reson. A 113 (1995) 108–113.
[5] D.M. Gregory, R.E. Gerald II, R.E. Botto, J. Magn. Reson. 131 (1998) 327–335.
[6] D.M. Schmidt, J.S. George, S.I. Penttila, A. Caprihan, E. Fukushima, J. Magn. Reson. 129 (1997) 184–187.
[7] I.L. Moudrakovski, A. Sanchez, C.I. Ratcliffe, J.A. Ripmeester, J. Phys. Chem. B 104 (2000) 7306–7310.
[8] Y.-Q. Song, H.C. Gaede, T. Pietrass, G.A. Barrall, G.C. Chingas, G.C. Ayers, A. Pines, J. Magn. Reson. A 115 (1995) 127–130.
[9] Y.-Q. Song, B.M. Goodson, B. Sheridan, T.M. de Swiet, A. Pines, J. Chem. Phys. 108 (1998) 6233–6239.
[10] P.T. Callaghan, Principles of Nuclear Magnetic Resonance Microscopy, Clarendon Press, Oxford, 1995.
[11] K.J. Packer, J.J. Tessier, Mol. Phys. 87 (1996) 267–272.
[12] M. Hallman, K.K. Unger, M. Appel, G. Fleischer, J. Karger, J. Phys. Chem. 100 (1996) 7729–7734.
[13] R.Q. Snurr, A. Hagen, H. Ernst, H.B. Schwarz, S. Ernst, J. Weitkamp, J. Karger, J. Catal. 163 (1996) 130–137.
[14] M.P. Hollewand, L.F. Gladden, Chem. Eng. Sci. 50 (1995) 309–326.
[15] P.T. Callaghan, Y. Xia, J. Magn. Reson. 91 (1991) 326–352.
[16] J. Stepisnik, Prog. NMR Spectrosc. 17 (1985) 187–209.
[17] J.D. Seymour, P.T. Callaghan, AIChE J. 43 (1997) 2096–2111.
[18] A. Feinauer, S.A. Altobelli, E. Fukushima, Magn. Reson. Imaging 15 (1997) 479–487.
[19] E. Fukushima, Annu. Rev. Fluid Mech. 31 (1999) 95–123.
[20] S.-I. Han, B. Blumich, Appl. Magn. Reson. 18 (2000) 101–114.
[21] U. Hong, J. Karger, B. Hunger, N.N. Feoktistova, S.P. Zhdanov, J. Catal. 137 (1992) 243–251.
[22] E. Brunner, M. Haake, L. Kaiser, A. Pines, J.A. Reimer, J. Magn. Reson. 138 (1999) 155–159.
[23] P.J. Prado, B.J. Balcom, I.V. Mastikhin, A.R. Cross, R.L. Armstrong, A. Logan, J. Magn. Reson. 137 (1999) 324–332.
[24] M.J. Lizak, M.S. Conradi, C.G. Fry, J. Magn. Reson. 95 (1991) 548–557.
[25] I.V. Koptyug, S.A. Altobelli, E. Fukushima, A.V. Matveev, R.Z. Sagdeev, J. Magn. Reson. 147 (2000) 36–42.
[26] A. Caprihan, E. Fukushima, Phys. Rep. 198 (1990) 195–235.
[27] S. Gravina, D.G. Cory, J. Magn. Reson. B 104 (1994) 53–61.
[28] S. Choi, X. Tang, D.G. Cory, Int. J. Imaging Syst. Technol. 8 (1997) 263–276.
[29] I.V. Koptyug, R.Z. Sagdeev, L.Yu. Khitrina, V.N. Parmon, Appl. Magn. Reson. 18 (2000) 13–28.